Transport coefficients for electrolytes in arbitrarily shaped nano- and microfluidic channels

N A Mortensen[1], L H Olesen and H Bruus

MIC—Department of Micro and Nanotechnology, NanoDTU,
Technical University of Denmark, Bld. 345 east,
DK-2800 Kongens Lyngby, Denmark
E-mail: nam@mic.dtu.dk

Abstract. We consider laminar flow of incompressible electrolytes in long, straight channels driven by pressure and electro-osmosis. We use a Hilbert space eigenfunction expansion to address the general problem of an arbitrary cross-section and obtain general results in linear-response theory for the hydraulic and electrical transport coefficients which satisfy Onsager relations. In the limit of non-overlapping Debye layers, the transport coefficients are simply expressed in terms of parameters of the electrolyte as well as the geometrical correction factor for the Hagen–Poiseuille part of the problem. In particular, we consider the limits of thin non-overlapping as well as strongly overlapping Debye layers, respectively, and calculate the corrections to the hydraulic resistance due to electro-hydrodynamic interactions.

[1] Author to whom any correspondence should be addressed.

Contents

1. Introduction

Laminar Hagen–Poiseuille and electro-osmotic flow is important to a variety of lab-on-a-chip applications and microfluidics [1]–[3] and the rapid development of micro- and nano-fabrication techniques during the past decade has put even more emphasis on flow in channels with a variety of shapes depending on the fabrication technique in use. The list of examples includes rectangular channels obtained by hot embossing in polymer wafers, semi-circular channels in isotropically etched surfaces, triangular channels in KOH-etched silicon crystals, Gaussian-shaped channels in laser-ablated polymer films, and elliptic channels in stretched PDMS devices [4]. While general results for the shape dependence of the hydraulic resistance in the case of a non-conducting fluid were reported recently [5] there has been, according to our knowledge, no analogous detailed study of the shape dependence of flow of electrolytes in the presence of a zeta potential which is a scenario of key importance to lab-on-a-chip applications involving biological liquids/samples in both microfluidic [6]–[8] and nanofluidic channels [9]–[14].

In this paper we address the general steady-state flow problem in figure 1 where pressure gradients and electro-osmosis (EO) are playing in concert [15]. We consider a long, straight channel of length L having a constant cross-section Ω of area $\mathcal{A}$ and boundary $\partial\Omega$ of length $\mathcal{P}$. The channel contains an incompressible electrolyte, which we for simplicity assume to be binary and symmetric, i.e., containing ions of charge $+Ze$ and $-Ze$ and equal diffusivities D. The electrolyte has the Debye screening length λ_D, bulk conductivity σ_o, viscosity η, permittivity ϵ and at the boundary $\partial\Omega$ it has a zeta potential ζ. The laminar, steady-state flow is driven by a linear pressure drop Δp and a linear voltage drop ΔV. With these definitions flow will be in the positive x-direction. In the linear-response regime the corresponding volume flow rate Q and charge current I are related to the driving fields by

$$\begin{pmatrix} Q \\ I \end{pmatrix} = G \begin{pmatrix} \Delta p \\ \Delta V \end{pmatrix}, \qquad G = \begin{pmatrix} G_{11} & G_{12} \\ G_{21} & G_{22} \end{pmatrix}, \tag{1}$$
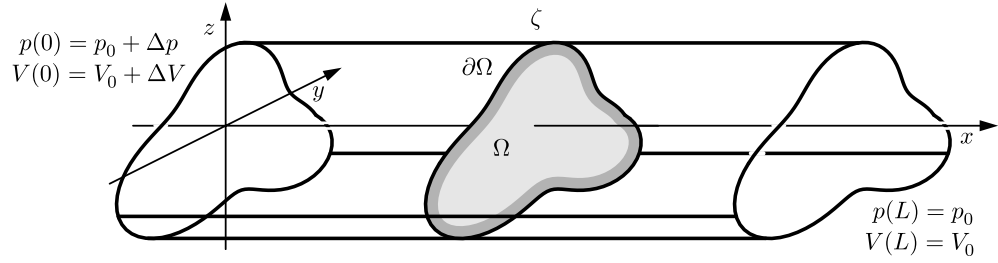
Figure 1. A translation invariant channel of arbitrary cross-section Ω of area $\mathcal{A}$ containing an electrolyte driven by a pressure gradient $-\Delta p/L$ and by electro-osmosis through the potential gradient $-\Delta V/L$. The channel wall $\partial\Omega$ has the electrical potential ζ, which induces a thin, charged Debye layer (dark grey) that surrounds the charge neutral bulk (light grey).

where, according to Onsager relations [16], G is a symmetric, $G_{12} = G_{21}$, two-by-two conductance matrix. The upper diagonal element is the hydraulic conductance or inverse hydraulic resistance given by

$$G_{11} = \frac{\mathcal{A}}{\alpha\eta}\frac{\mathcal{A}}{L}, \tag{2}$$

where α is the dimensionless geometrical correction factor, shown in [5] to be a linear function of the dimensionless compactness parameter $\mathcal{C} = \mathcal{P}^2/\mathcal{A}$. While there is no intrinsic length scale influencing G_{11}, the other elements of G depend on the Debye screening length λ_D. This length can be comparable to and even exceed the transverse dimensions in nano-channels [9]–[11], in which case the off-diagonal elements may depend strongly on the actual cross-sectional geometry. However, for thin Debye layers with a vanishing overlap the matrix elements G_{12}, G_{21} and G_{22} are independent of the details of the geometry. For a free electro-osmotic flow, a constant velocity field $v_{\mathrm{eo}} = (\epsilon\zeta/\eta)\Delta V/L$ is established throughout the channel, except for in the thin Debye layer of vanishing width. Hence, $Q = v_{\mathrm{eo}}\mathcal{A}$ and

$$G_{12} = G_{21} = -\frac{\epsilon\zeta}{\eta}\frac{\mathcal{A}}{L}, \qquad \lambda_D \ll \frac{\mathcal{A}}{\mathcal{P}}. \tag{3}$$

From Ohm's law $I = (\sigma_{\mathrm{o}}\mathcal{A}/L)\Delta V$, it follows that

$$G_{22} = \sigma_{\mathrm{o}}\frac{\mathcal{A}}{L}, \qquad \lambda_D \ll \frac{\mathcal{A}}{\mathcal{P}}. \tag{4}$$

For strongly overlapping Debye layers we find (see sections 3.2.2 and 4.2) that

$$G_{12} = G_{21} = -\frac{\epsilon\zeta}{\eta}\frac{\sinh\left(\frac{Ze\zeta}{k_BT}\right)}{\frac{Ze\zeta}{k_BT}}\frac{\mathcal{A}}{\alpha\lambda_D^2}\frac{\mathcal{A}}{L}, \qquad \lambda_D \gg \frac{\mathcal{A}}{\mathcal{P}}, \tag{5}$$

$$G_{22} = \left[\cosh\left(\frac{Ze\zeta}{k_BT}\right) + \frac{\epsilon\zeta^2}{\eta D}\frac{\sinh^2\left(\frac{Ze\zeta}{k_BT}\right)}{\left(\frac{Ze\zeta}{k_BT}\right)^2}\frac{\mathcal{A}}{\alpha\lambda_D^2}\right]\sigma_{\mathrm{o}}\frac{\mathcal{A}}{L}, \qquad \lambda_D \gg \frac{\mathcal{A}}{\mathcal{P}}. \tag{6}$$

We emphasize that the above results are generally valid for symmetric electrolytes, even beyond the Debye–Hückel approximation. In the Debye–Hückel limit $Ze\zeta \ll k_B T$ they also hold for asymmetric electrolytes. We also note that in the Debye–Hückel limit the expressions agree fully with the corresponding limits for a circular cross-section and the infinite parallel plate system, where explicit solutions exist in the Debye–Hückel limit in terms of Bessel functions [17, 18] and cosine hyperbolic functions [18], respectively. From the corresponding resistance matrix $R = G^{-1}$, we get the hydraulic resistance

$$R_{11} = \frac{\alpha}{1-\beta} \frac{\eta L}{\mathcal{A}^2}, \tag{7}$$

where $\beta \equiv G_{12}G_{21}/(G_{11}G_{22})$ is the Debye-layer correction factor to the hydraulic resistance. In the two limits, we have

$$\beta \simeq \alpha \frac{\epsilon^2 \zeta^2}{\eta \sigma_\circ \mathcal{A}} \times \begin{cases} 1, & \lambda_D \ll \dfrac{\mathcal{A}}{\mathcal{P}} \\[2ex] \left(\dfrac{Ze\zeta}{k_B T}\right)^{-1} \sinh\left(\dfrac{Ze\zeta}{k_B T}\right)\left(\dfrac{\mathcal{A}}{\alpha \lambda_D^2}\right)^2, & \lambda_D \gg \dfrac{\mathcal{A}}{\mathcal{P}} \end{cases}. \tag{8}$$

For ζ going to zero β vanishes and we recover the result in [5] for the hydraulic resistance.

2. Governing equations

For the system illustrated in figure 1, an external pressure gradient $\vec{\nabla} p = -(\Delta p/L)\vec{e}_x$ and an external electrical field $\vec{E} = E\vec{e}_x = (\Delta V/L)\vec{e}_x$ is applied. There is full translation invariance along the x-axis, from which it follows that the velocity field is of the form $\vec{v}(\vec{r}) = v(\vec{r}_\perp)\vec{e}_x$ where $\vec{r}_\perp = y\vec{e}_y + z\vec{e}_z$. For the equilibrium potential and the corresponding charge density, we have $\phi_{eq}(\vec{r}) = \phi_{eq}(\vec{r}_\perp)$ and $\rho_{eq}^e(\vec{r}) = \rho_{eq}^e(\vec{r}_\perp)$, respectively. We follow our related recent works [19, 20] and use the Dirac *bra-ket* notation [21, 22], where functions $f(\vec{r}_\perp)$ in Ω are written as $|f\rangle$ with inner products defined by the cross-section integral

$$\langle f|g\rangle \equiv \int_\Omega \mathrm{d}\vec{r}_\perp \, f(\vec{r}_\perp) g(\vec{r}_\perp). \tag{9}$$

From the Navier–Stokes equation it follows that the velocity is governed by [23, 24]

$$0 = \frac{\Delta p}{L}|1\rangle + \eta \nabla_\perp^2 |v\rangle + \frac{\Delta V}{L}|\rho_{eq}^e\rangle, \tag{10}$$

where $\nabla_\perp^2 = \partial_y^2 + \partial_z^2$ is the two-dimensional Laplacian. The equilibrium potential $|\phi_{eq}\rangle$ and the charge density $|\rho_{eq}^e\rangle$ are related by the Poisson equation

$$\nabla_\perp^2 |\phi_{eq}\rangle = -\frac{1}{\epsilon}|\rho_{eq}^e\rangle. \tag{11}$$

The velocity $|v\rangle$ is subject to a no-slip boundary condition on $\partial\Omega$ while the equilibrium potential $|\phi_{eq}\rangle$ equals the zeta potential ζ on $\partial\Omega$. Obviously, we also need a statistical model

for the electrolyte, and in the subsequent sections we will use the Boltzmann model where the equilibrium potential $|\phi_{eq}\rangle$ is governed by the Poisson–Boltzmann equation. However, before turning to a specific model we will first derive general results which are independent of the description of the electrolyte.

We first note that because equation (10) is linear we can decompose the velocity as $|v\rangle = |v_p\rangle + |v_{eo}\rangle$, where $|v_p\rangle$ is the Hagen–Poiseuille pressure driven velocity governed by

$$0 = \frac{\Delta p}{L}|1\rangle + \eta \nabla_\perp^2 |v_p\rangle \tag{12}$$

and $|v_{eo}\rangle$ is the electro-osmotic velocity given by

$$|v_{eo}\rangle = -\frac{\epsilon \Delta V}{\eta L}(\zeta|1\rangle - |\phi_{eq}\rangle). \tag{13}$$

The latter result is obtained by substituting equation (11) for $|\rho_{eq}^e\rangle$ in equation (10). The upper diagonal element in G is given by $G_{11} = \langle 1|v_p\rangle/\Delta p$ which may be parameterized according to equation (2). The upper off-diagonal element is given by $G_{12} = \langle 1|v_{eo}\rangle/\Delta V$ and combined with the Onsager relation, we get

$$G_{12} = G_{21} = -\frac{1}{L}\frac{\epsilon}{\eta}\langle 1|\zeta - \phi_{eq}\rangle = -\frac{\mathcal{A}}{L}\frac{\epsilon}{\eta}(\zeta - \bar{\phi}_{eq}), \tag{14}$$

where we have used that $\langle 1|1\rangle = \mathcal{A}$ and introduced the average potential $\bar{\phi}_{eq} = \langle\phi_{eq}|1\rangle/\langle 1|1\rangle$.

There are two contributions to the lower diagonal element G_{22}; one from migration, $G_{22}^{mig} = \langle 1|\sigma\rangle/L$, and one from electro-osmotic convection of charge, $G_{22}^{conv} = \langle\rho_{eq}^e|v_{eo}\rangle/\Delta V$, so that

$$G_{22} = G_{22}^{mig} + G_{22}^{conv} = \frac{1}{L}\langle 1|\sigma\rangle - \frac{\epsilon}{\eta L}\langle\rho_{eq}^e|\zeta - \phi_{eq}\rangle, \tag{15}$$

where the electrical conductivity $\sigma(\vec{r}_\perp)$ depends on the particular model for the electrolyte. For thin non-overlapping Debye layers, we note that $\bar{\phi}_{eq} \simeq 0$ so that equation (14) reduces to equation (3) and, similarly since the induced charge density is low, equation (15) reduces to equation (4). For strongly overlapping Debye layers, the weak screening means that ϕ_{eq} approaches ζ so that the off-diagonal elements $G_{12} = G_{21}$ and the G_{22}^{conv} part of G_{22} vanish entirely. In the following, we consider a particular model for the electrolyte and calculate the asymptotic suppression as a function of the Debye screening length λ_D.

3. Debye–Hückel approximation

In the Debye–Hückel approximation, the equilibrium potential $|\phi_{eq}\rangle$ is governed by the linearized Poisson–Boltzmann equation [3]

$$\nabla_\perp^2 |\phi_{eq}\rangle = \frac{1}{\lambda_D^2}|\phi_{eq}\rangle, \tag{16}$$

where λ_D is the Debye screening length. The validity of this model will be discussed in more detail in section 4.

3.1. Hilbert space formulation

In order to solve equations (10), (11) and (16) we will take advantage of the Hilbert space formulation [25], often employed in quantum mechanics [22], and recently employed by us on the problem of an accelerating Poiseuille flow [19]. The Hilbert space of real functions on Ω is defined by the inner product in equation (9) and a complete, countable set $\{|\psi_n\rangle\}$ of orthonormal basis functions, i.e.,

$$\langle \psi_m | \psi_n \rangle = \delta_{nm}, \tag{17}$$

where δ_{nm} is the Kronecker delta. We choose the eigenfunctions $\{|\psi_n\rangle\}$ of the Helmholtz equation (with a zero Dirichlet boundary condition on $\partial\Omega$) as our basis functions,

$$-\nabla_\perp^2 |\psi_n\rangle = \kappa_n^2 |\psi_n\rangle, \qquad n = 1, 2, 3, \ldots. \tag{18}$$

With this complete basis any function in the Hilbert space can be written as a linear combination of basis functions. In the following we write the fields as

$$|v\rangle = \sum_{n=1}^{\infty} a_n |\psi_n\rangle, \tag{19}$$

$$|\phi_{\text{eq}}\rangle = \zeta |1\rangle - \sum_{n=1}^{\infty} b_n |\psi_n\rangle, \tag{20}$$

$$|\rho_{\text{eq}}^e\rangle = \sum_{n=1}^{\infty} c_n |\psi_n\rangle. \tag{21}$$

Inserting equations (18) and (20) into equation (16), and multiplying by $\langle \psi_m |$, yields

$$b_n = \zeta \frac{\langle \psi_n | 1 \rangle}{1 + (\kappa_n \lambda_D)^2}, \quad n = 1, 2, 3, \ldots. \tag{22}$$

Likewise, inserting equations (18)–(21) and (22) into equation (11), and multiplying by $\langle \psi_m |$, yields

$$c_n = -\epsilon \zeta \kappa_n^2 \frac{\langle \psi_n | 1 \rangle}{1 + (\kappa_n \lambda_D)^2}, \qquad n = 1, 2, 3, \ldots. \tag{23}$$

Finally, using equations (19), (20), (22) and (23) in equation (10) leads to

$$a_n = \left(\frac{\Delta p}{\eta L} \frac{1}{\kappa_n^2} - \frac{\epsilon \zeta \Delta V}{\eta L} \frac{1}{1 + (\kappa_n \lambda_D)^2} \right) \langle \psi_n | 1 \rangle, \quad n = 1, 2, 3, \ldots. \tag{24}$$

3.2. Transport coefficients

The flow rate and the electrical current are conveniently written as

$$Q = \langle 1|v\rangle, \tag{25}$$

$$I = \langle \rho_{eq}^e|v\rangle + \sigma_o E\langle 1|1\rangle, \tag{26}$$

where the second relation is the linearized Nernst–Planck equation with the first term being the convection/streaming current, while the second is the ohmic current. Substituting equations (19) and (21) into these expressions, we identify the transport coefficients as

$$G_{11} = \frac{\mathcal{A}}{\eta L} \sum_{n=1}^{\infty} \frac{1}{\kappa_n^2} \frac{\mathcal{A}_n}{\mathcal{A}}, \tag{27}$$

$$G_{12} = -\frac{\epsilon\zeta\mathcal{A}}{\eta L} \sum_{n=1}^{\infty} \frac{1}{1 + (\kappa_n\lambda_D)^2} \frac{\mathcal{A}_n}{\mathcal{A}}, \tag{28}$$

$$G_{21} = -\frac{\epsilon\zeta\mathcal{A}}{\eta L} \sum_{n=1}^{\infty} \frac{1}{1 + (\kappa_n\lambda_D)^2} \frac{\mathcal{A}_n}{\mathcal{A}}, \tag{29}$$

$$G_{22} = \frac{\sigma_o\mathcal{A}}{L} + \frac{(\epsilon\zeta)^2}{\eta\lambda_D^2} \frac{\mathcal{A}}{L} \sum_{n=1}^{\infty} \frac{(\kappa_n\lambda_D)^2}{[1 + (\kappa_n\lambda_D)^2]^2} \frac{\mathcal{A}_n}{\mathcal{A}}, \tag{30}$$

where

$$\mathcal{A}_n \equiv \frac{|\langle 1|\psi_n\rangle|^2}{\langle\psi_n|\psi_n\rangle} = |\langle 1|\psi_n\rangle|^2 \tag{31}$$

is the effective area of the eigenfunction $|\psi_n\rangle$. The fraction $\mathcal{A}_n/\mathcal{A}$ is consequently a measure of the relative area occupied by $|\psi_n\rangle$ satisfying the sum-rule $\sum_{n=1}^{\infty} \mathcal{A}_n = \mathcal{A}$ [19]. We note that as expected G obeys the Onsager relation $G_{12} = G_{21}$. Furthermore, using that

$$\frac{(\kappa_n\lambda_D)^2}{[1 + (\kappa_n\lambda_D)^2]^2} = -\frac{\lambda_D}{2} \frac{\partial}{\partial\lambda_D} \frac{1}{1 + (\kappa_n\lambda_D)^2}, \tag{32}$$

we get the following bound between the off-diagonal elements $G_{12} = G_{21}$ and the lower diagonal element G_{22},

$$G_{22} = \frac{\sigma_o\mathcal{A}}{L} + \frac{\epsilon\zeta}{2\lambda_D} \frac{\partial G_{12}}{\partial\lambda_D}. \tag{33}$$

Table 1. Central dimensionless parameters for different geometries.

	k_1^2	$\mathcal{A}_1^{\mathrm{eff}}/\mathcal{A}$	α	$\alpha/\mathcal{C}$
Circle	$\gamma_1^2/4 \simeq 1.45$[a,b]	$4/\gamma_1^2 \simeq 0.69$[a,b]	4π	2[c]
Quarter-circle	1.27[d]	0.65[d]	29.97[d]	1.85[d]
Half-circle	1.38[d]	0.64[d]	33.17[d]	1.97[d]
Ellipse (1:2)	1.50[d]	0.67[d]	10π[c]	2.10[d]
Ellipse (1:3)	1.54[d]	0.62[d]	$40\pi/3$[c]	2.21[d]
Ellipse (1:4)	1.57[d]	0.58[d]	17π[c]	2.28[d]
Triangle (1:1:1)	$\pi^2/9 \simeq 1.10$[e]	$6/\pi^2 \simeq 0.61$[e]	$20\sqrt{3}$[c]	$5/3 \simeq 1.67$[c]
Triangle (1:1:$\sqrt{2}$)	$\frac{5\pi^2}{4(2+\sqrt{2})^2} \simeq 1.06$[a]	$512/9\pi^4 \simeq 0.58$[a]	38.33[d]	1.64[d]
Square (1:1)	$\pi^2/8 \simeq 1.23$[a]	$64/\pi^4 \simeq 0.66$[a]	28.45[d]	1.78[d]
Rectangle (1:2)	$5\pi^2/36 \simeq 1.37$[a]	$64/\pi^4 \simeq 0.66$[a]	34.98[d]	1.94[d]
Rectangle (1:3)	$5\pi^2/32 \simeq 1.54$[a]	$64/\pi^4 \simeq 0.66$[a]	45.57[d]	2.14[d]
Rectangle (1:4)	$17\pi^2/100 \simeq 1.68$[a]	$64/\pi^4 \simeq 0.66$[a]	56.98[d]	2.28[d]
Rectangle(1:∞)	$\sim\pi^2/4 \simeq 2.47$[a]	$64/\pi^4 \simeq 0.66$[a]	∞	~ 3[f]
Pentagon	1.30[d]	0.67[d]	26.77[d]	1.84[d]
Hexagon	1.34[d]	0.68[d]	26.08[d]	1.88[d]

[a]See e.g. [25] for the eigenmodes and eigenspectrum.
[b]Here, $\gamma_1 \simeq 2.405$ is the first root of the zeroth Bessel function of the first kind.
[c]See e.g. [5] and references therein.
[d]Data obtained by finite-element simulations [26].
[e]See e.g. [28] for the eigenmodes and eigenspectrum.
[f]See e.g. [23] for a solution of the Poisson equation.

In the context of the geometrical correction factor α studied in detail in [5] we note that the first diagonal element may be written as $G_{11} = G_{11}^*/\alpha$, where $G_{11}^* = \frac{\mathcal{A}^2}{\eta L}$ is a characteristic hydraulic conductance and the geometrical correction factor α can be expressed as [19]

$$\alpha \equiv \left(\sum_{n=1}^{\infty} \frac{1}{\kappa_n^2 \mathcal{A}} \frac{\mathcal{A}_n}{\mathcal{A}}\right)^{-1} = \mathcal{C}\left(\sum_{n=1}^{\infty} \frac{1}{k_n^2} \frac{\mathcal{A}_n}{\mathcal{A}}\right)^{-1}, \tag{34}$$

where $k_n = \kappa_n \mathcal{A}/\mathcal{P}$ is a dimensionless eigenvalue. In passing we furthermore note that this formal result is a convenient starting point for perturbative analysis of the correction due to small changes in the boundary $\partial\Omega$ [25].

3.2.1. Non-overlapping, thin Debye layers. For the off-diagonal elements of G we use that $[1 + (\kappa_n \lambda_D)^2]^{-1} = 1 + \mathcal{O}[k_n^2(\lambda_D \mathcal{P}/\mathcal{A})^2]$. In section 5, we numerically justify that the smallest dimensionless eigenvalue k_1^2 is of the order unity, so we may approximate the sum by a factor of unity, see table 1, whereby we arrive at equation (3) for $\lambda_D \ll \mathcal{A}/\mathcal{P}$. These results for the off-diagonal elements are fully equivalent to the Helmholtz–Smoluchowski result [18]. For G_{22} we use that $(\kappa_n \lambda_D)^2[1 + (\kappa_n \lambda_D)^2]^{-2} = \mathcal{O}[k_n^2(\lambda_D \mathcal{P}/\mathcal{A})^2]$, thus we may neglect the second term, whereby we arrive at equation (4).

3.2.2. Strongly overlapping Debye layers. In the case of $\kappa_1 \lambda_D \gg 1$ we may use the result $[1 + (\kappa_n \lambda_D)^2]^{-1} = (\kappa_n \lambda_D)^{-2} + \mathcal{O}[k_n^{-4}(\lambda_D \mathcal{P}/\mathcal{A})^{-4}]$, which gives

$$G_{12} = G_{21} \simeq -\frac{\epsilon \zeta}{\lambda_D^2} G_{11}, \qquad \lambda_D \gg \frac{\mathcal{A}}{\mathcal{P}}. \tag{35}$$

This is the Debye–Hückel limit of equation (5) for strongly overlapping Debye layers. For G_{22}, we use equation (33) and arrive at the result in equation (6) for $Ze\zeta \ll k_B T$ by using $\sigma_{\mathrm{o}} = \epsilon D/\lambda_D^2$.

3.2.3. The circular case. For a circular cross-section, where $\alpha = 8\pi$, it can be shown that [18]

$$G_{12}^{\mathrm{circ}} = G_{21}^{\mathrm{circ}} = -\frac{\mathcal{A}}{L} \frac{\epsilon \zeta}{\eta} \frac{I_2(\sqrt{8\mathcal{A}/\alpha \lambda_D^2})}{I_0(\sqrt{8\mathcal{A}/\alpha \lambda_D^2})}, \tag{36}$$

where I_n is the nth modified Bessel function of the first kind, and where we have explicitly introduced the variable $\mathcal{A}/\alpha \lambda_D^2$ to emphasize the asymptotic dependence in equation (5) for strongly overlapping Debye layers. We note that we recover the limits in equations (3) and (5) for $\lambda_D \ll \mathcal{A}/\mathcal{P}$ and $\lambda_D \gg \mathcal{A}/\mathcal{P}$, respectively.

4. Beyond the Debye–Hükel approximation

In order to go beyond the Debye–Hückel approximation we consider, for simplicity, a symmetric binary $(Z : Z)$ electrolyte. Next, we neglect strong correlations between the ions so that the equilibrium properties of the electrolyte are governed by Boltzmann statistics [3], i.e., the concentrations of the two type of ions are given by

$$c_{\mathrm{eq}}^{\pm}(\vec{r}_\perp) = c_{\mathrm{o}} \exp\left[\mp \frac{Ze}{k_B T} \phi_{\mathrm{eq}}(\vec{r}_\perp)\right]. \tag{37}$$

This is equivalent to assuming equilibrium with bulk reservoirs at the ends of the channel in which the potential ϕ_{eq} tends to zero and both concentrations $c_{\mathrm{eq}}^{\pm}$ to c_{o}.

Substituting the charge density $\rho_{\mathrm{eq}}^e = Ze(c_{\mathrm{eq}}^+ - c_{\mathrm{eq}}^-)$ into the Poisson equation (11), we arrive at the nonlinear Poisson–Boltzmann equation [3, 18]

$$\nabla_\perp \phi_{\mathrm{eq}}(\vec{r}_\perp) = \frac{k_B T}{Ze\lambda_D^2} \sinh\left[\frac{Ze}{k_B T} \phi_{\mathrm{eq}}(\vec{r}_\perp)\right], \tag{38}$$

where the Debye screening length is given by

$$\lambda_D = \sqrt{\frac{\epsilon k_B T}{2(Ze)^2 c_{\mathrm{o}}}}. \tag{39}$$

The conductivity σ of the electrolyte depends on the local ionic concentrations

$$\sigma(\vec{r}_\perp) = \frac{(Ze)^2 D}{k_B T}[c_{\mathrm{eq}}^+(\vec{r}_\perp) + c_{\mathrm{eq}}^-(\vec{r}_\perp)] = \sigma_{\mathrm{o}} \cosh\left[\frac{Ze}{k_B T} \phi_{\mathrm{eq}}(\vec{r}_\perp)\right], \tag{40}$$

assuming equal diffusivities D for the two ionic species. In the Debye–Hückel limit, $Ze\zeta \ll k_B T$, where thermal energy dominates over the electrostatic energy we may linearize the right-hand side of equation (38) so that we arrive at the Debye–Hückel approximation in equation (16). Similarly the conductivity in equation (40) reduces to the bulk conductivity σ_o. Compared to equation (26) the electrical current obtained from the nonlinear Nernst–Planck equation becomes

$$I = \langle \rho^e_{eq} | v \rangle + E \langle \sigma | 1 \rangle. \tag{41}$$

We calculate the off-diagonal elements from $G_{12} = G_{21} = \langle \rho^e_{eq} | v_p \rangle / \Delta p$ and find

$$G_{12} = G_{21} = -\frac{1}{\Delta p} \frac{\epsilon k_B T}{Ze\lambda_D^2} \left\langle \sinh\left(\frac{Ze}{k_B T}\phi_{eq}\right) \middle| v_p \right\rangle. \tag{42}$$

Similarly, from equation (15) for the two components in the electrical conduction $G_{22} = G_{22}^{mig} + G_{22}^{conv}$, we get

$$G_{22}^{mig} = \frac{\sigma_o}{L} \left\langle \cosh\left(\frac{Ze}{k_B T}\phi_{eq}\right) \middle| 1 \right\rangle, \tag{43}$$

$$G_{22}^{conv} = \frac{\sigma_o m}{2L} \frac{Ze}{k_B T} \left\langle \sinh\left(\frac{Ze}{k_B T}\phi_{eq}\right) \middle| \zeta - \phi_{eq} \right\rangle, \tag{44}$$

where we have used that $\sigma_o = \epsilon D / \lambda_D^2$ and introduced the dimensionless quantity m,

$$m \equiv \left(\frac{k_B T}{Ze}\right)^2 \frac{2\epsilon}{\eta D}, \tag{45}$$

which indicates the importance of electro-osmosis relative to electro-migration.

4.1. Non-overlapping, thin Debye layers

In the limit of thin Debye layers, we have already discussed how equation (14) in general leads to equation (3) because the screening is good and ϕ_{eq} is nonzero only on a negligible part of Ω. This property is more implicit when G_{12} or G_{21} is written in the form of equation (42), which is a more appropriate starting point for analysing the limit of strongly overlapping Debye layers. For G_{22} the calculations are more involved; we assume that the channel wall is sufficiently smooth on the Debye-length scale so that we can everywhere use the Gouy–Chapman (GC) solution for a semi-infinite planar geometry [3, 18],

$$\phi_{eq}^{GC} = \frac{k_B T}{Ze} 4 \tanh^{-1}\left[\tanh\left(\frac{Ze\zeta}{4k_B T}\right) e^{-r_n/\lambda_D}\right], \tag{46}$$

where r_n denotes the normal distance to the channel wall. Substituting this into equations (43) and (44) the integrals can be carried out analytically resulting in

$$G_{22} = \sigma_o \frac{\mathcal{A}}{L}(1 + Du), \qquad \lambda_D \ll \frac{\mathcal{A}}{\mathcal{P}}, \tag{47}$$

where Du is the Dukhin number

$$Du = \frac{\lambda_D \mathcal{P}}{\mathcal{A}}(1 + m)\, 4 \sinh^2\left(\frac{Ze\zeta}{4 k_B T}\right), \tag{48}$$

defined as the ratio of the surface conductivity in the charged Debye layers to the bulk conductivity σ_o times the geometrical length scale $\mathcal{A}/\mathcal{P}$ (see [29] and references therein). Clearly, when the Debye layer becomes very thin, surface conduction is negligible, we recover the simple result in equation (4).

4.2. Strongly overlapping Debye layers

When the Debye layers are strongly overlapping the screening is weak and $\phi_{eq} \approx \zeta$ throughout the cross-section. Hence, we can pull the integrand $\sinh(Ze\phi_{eq}/k_B T)$ outside the *bra-ket* in equation (42) and we arrive at equation (5). Here, we have used that $\langle 1|v_p\rangle/\Delta p = G_{11}$ and introduced the parameterization in equation (2). Similarly, from equations (43) and (44) we obtain equation (6) where we have used equations (14) and (5) to eliminate $\langle 1|\zeta - \phi_{eq}\rangle$.

 We note that due to shifts in free energies, the zeta potential inside a narrow channel with significant Debye-layer overlap is generally not the same as in a macroscopic channel with no overlap, see e.g. [11, 30] for a discussion.

5. Numerical results

5.1. The Helmholtz basis

Only few geometries allow analytical solutions of both the Helmholtz equation and the Poisson equation. The circle is of course among the most well-known solutions and the equilateral triangle is another example. However, in general the equations have to be solved numerically, and for this purpose we have used the commercially available finite-element software Femlab [27]. The first eigenstate of the Helmholtz equation is in general non-degenerate and numbers for a selection of geometries are tabulated in table 1. Note how the different numbers converge when going through the regular polygons starting from the equilateral triangle through the square, the regular pentagon, and the regular hexagon to the circle. In general, k_1^2 is of the order unity, and for relevant high-order modes (those with a nonzero $\mathcal{A}_n$) the eigenvalue is typically much larger. Similarly, for the effective area we find that $\mathcal{A}_1/\mathcal{A} \leqslant 4/\gamma_1^2 \simeq 0.69$ and consequently we have $\mathcal{A}_n/\mathcal{A} < 1 - 4/\gamma_1^2 \simeq 0.31$ for $n \geq 2$. The transport coefficients in equations (27)–(30) are thus strongly influenced by the first eigenmode which may be used for approximations and estimates of the transport coefficients. As an example, the column for $\alpha/\mathcal{C}$ is well approximated by only including the first eigenvalue in the summation in equation (34).

5.2. Transport coefficients

Our analytical results predict that when going to either of the limits of thin non-overlapping or strongly overlapping Debye layers, the transport coefficients only depend on the channel geometry through the cross-sectional area $\mathcal{A}$ and the correction factor α. Therefore, when plotted against the rescaled Debye length $\sqrt{\alpha/\mathcal{A}}\,\lambda_D$, all our results should collapse on the same asymptotes in the two limits.
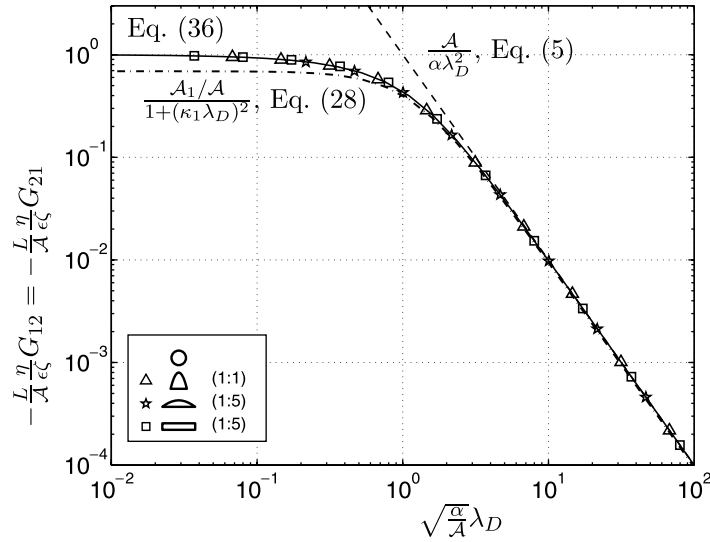
Figure 2. Rescaled off-diagonal transport coefficients versus rescaled Debye-layer thickness in the Debye–Hückel limit. The solid line is the exact result for a circle, equation (36), and the dashed line shows equation (5) for $Ze\zeta \ll k_B T$. The data points are finite-element simulations in the linearized regime for different cross-sections, see inset. Finally, the dash-dotted line shows the first term from the summation in equation (28) only.

In figure 2, we show the results for the off-diagonal coefficients obtained from finite-element simulations in the Debye–Hückel limit $Ze\zeta \ll k_B T$ for three different channel cross-sections, namely two parabola-shaped channels of aspect ratio 1 : 1 and 1 : 5, respectively, and a rectangular channel of aspect ratio 1 : 5. In all cases, we find excellent agreement between the numerics and the asymptotic expressions. For the comparison we have also included exact results, equation (36), for the circular cross-section as well as results based on only the first eigenvalue in equation (28). Even though equation (36) is derived for a circular geometry, we find that it also accounts remarkably well for even highly non-circular geometries in the intermediate regime of weakly overlapping Debye layers.

In figure 3, we show numerical results for the off-diagonal transport coefficients beyond the Debye–Hückel approximation. At large zeta potentials, the Debye layer is strongly compressed and the effective screening length reduced. Therefore, the suppression of the electro-osmotic flow/streaming current at strong Debye-layer overlap is shifted to larger values of λ_D as compared to the Debye–Hückel limit. For the comparison, we have also included the exact result for a circular cross-section in the Debye–Hückel approximation as well as the asymptotic expression for non-overlapping and strongly overlapping Debye layers, equation (5). As seen, the asymptotic expressions account well for the full numerical solutions independently of the geometry.

In figure 4, we show numerical results for the electrical conductance beyond the Debye–Hückel approximation. Open symbols show the electro-migration part G_{22}^{mig}, subtracted the trivial bulk contribution $\sigma_o \mathcal{A}/L$, whereas solid symbols show the electro-osmotic convection part G_{22}^{conv}, see equations (43) and (44), respectively. Again, we find that the numerics are in excellent agreement with our asymptotic results. For the $\lambda_D \ll \mathcal{P}/\mathcal{A}$ regime, we note that the Dukhin
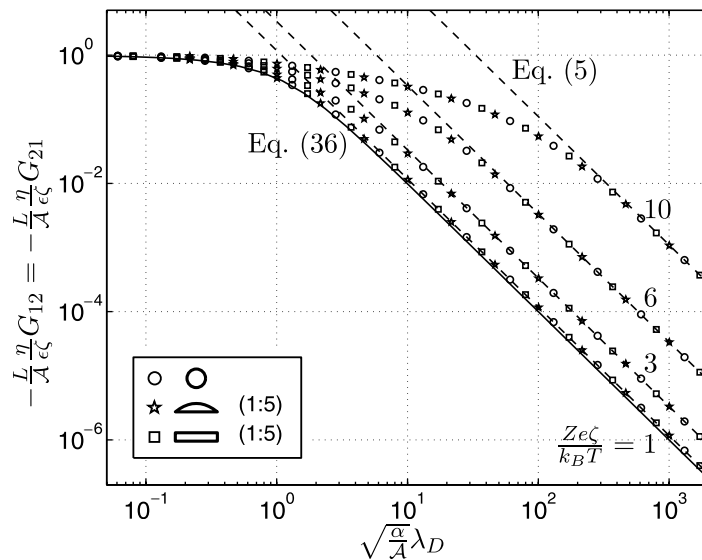
Figure 3. Rescaled off-diagonal transport coefficients versus rescaled Debye-layer thickness beyond the Debye–Hückel approximation. The solid line is the exact result for a circle within the Debye–Hückel approximation, equation (36). The data points are finite-element simulations for different cross-sections (see inset) with $Ze\zeta/k_BT = 1$, 3, 6 and 10 from below. The dashed lines indicate the corresponding asymptotic expression for strong Debye-layer overlap, equation (5).

number, equation (48), is proportional to $\lambda_D \mathcal{P}/\mathcal{A} = \sqrt{\mathcal{C}/\mathcal{A}}\,\lambda_D$ and not $\sqrt{\alpha/\mathcal{A}}\,\lambda_D$. Therefore, strictly one would not in general expect data to collapse on the same asymptote for $\lambda_D \ll \mathcal{P}/\mathcal{A}$. Looking carefully at this part of the figure, small variations can be seen from geometry to geometry—the reason why the variations are still so small is that $\alpha/\mathcal{C} \sim 2$ independently of geometry, see table 1.

6. Conclusion

We have analysed the flow of incompressible electrolytes in long, straight channels driven by pressure and EO. By using a powerful Hilbert space eigenfunction expansion, we have been able to address the general problem of an arbitrary cross-section and obtained general results for the hydraulic and electrical transport coefficients. Results for strongly overlapping and thin, non-overlapping Debye layers are particular simple, and from these analytical results we have calculated the corrections to the hydraulic resistance due to electro-hydrodynamic interactions. These analytical results reveal that the geometry dependence only appears through the area $\mathcal{A}$ and the correction factor α, as the expressions only depend on the rescaled Debye length $\sqrt{\alpha/\mathcal{A}}\,\lambda_D$. Our numerical analysis based on finite-element simulations indicates that these conclusions are generally valid also for intermediate values of λ_D. Combined with recent detailed work on the geometrical correction factor [5], the present results constitute an important step toward circuit

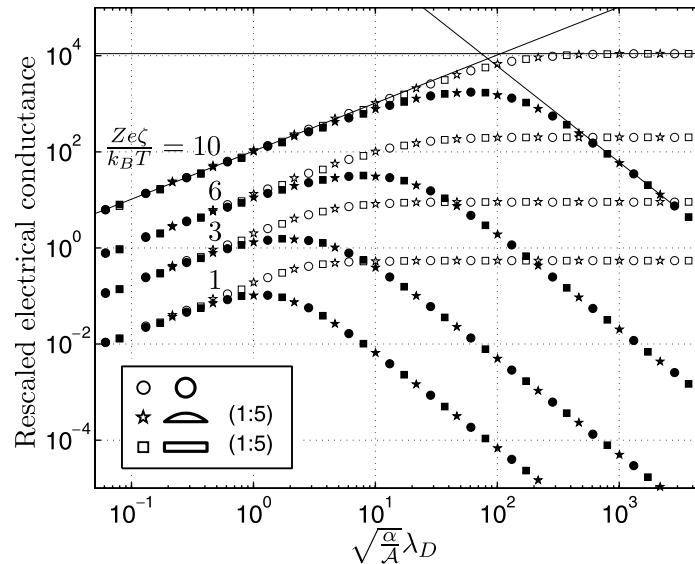**Figure 4.** Comparison of the two components in the G_{22} transport coefficient for three different geometries, see inset. Open symbols show $(G_{22}^{\mathrm{mig}} L/\sigma_{\mathrm{o}}\mathcal{A}) - 1$, i.e., the surface specific contribution to the electrical conductance from electro-migration, see equation (43). Solid symbols show the contribution from electro-osmotic convection $G_{22}^{\mathrm{conv}} L/m\sigma_{\mathrm{o}}\mathcal{A}$, see equation (44); for ease of comparison we have included the dimensionless number m in the rescaling. The data are obtained from finite-element simulations for different cross-sections (see inset) with $Ze\zeta/k_B T = 1,\ 3,\ 6$ and 10. The solid lines indicate the corresponding asymptotic expressions for strong and weak Debye-layer overlap, equations (6) and (47), respectively, for $Ze\zeta/k_B T = 10$ in a circular channel. Asymptotes for the other values of $Ze\zeta/k_B T$ have been left out for clarity, but equally good agreement is found also in these cases.

analysis [15] of complicated micro- and nanofluidic networks incorporating complicated cross-sectional channel geometries.

References

[1] Laser D J and Santiago J G 2004 *J. Micromech. Microeng.* **14** R35–64
[2] Stone H A, Stroock A D and Ajdari A 2004 *Annu. Rev. Fluid Mech.* **36** 381–411
[3] Squires T M and Quake S R 2005 *Rev. Mod. Phys.* **77** 977–1026
[4] Geschke O, Klank H and Telleman P (ed) 2004 *Microsystem Engineering of Lab-on-a-Chip Devices* (Weinheim: Wiley-VCH)
[5] Mortensen N A, Okkels F and Bruus H 2005 *Phys. Rev.* E **71** 057301
[6] Schasfoort R B M, Schlautmann S, Hendrikse L and van den Berg A 1999 *Science* **286** 942–5
[7] Takamura Y, Onoda H, Inokuchi H, Adachi S, Oki A and Horiike Y 2003 *Electrophoresis* **24** 185–92
[8] Reichmuth D S, Chirica G S and Kirby B J 2003 *Sens. Actuator B-Chem.* **92** 37–43
[9] Daiguji H, Yang P D, Szeri A J and Majumdar A 2004 *Nano Lett.* **4** 2315–21
[10] Stein D, Kruithof M and Dekker C 2004 *Phys. Rev. Lett.* **93** 035901

Institute *of* **Physics** ⏀ DEUTSCHE PHYSIKALISCHE GESELLSCHAFT

[11] van der Heyden F H J, Stein D and Dekker C 2005 *Phys. Rev. Lett.* **95** 116104
[12] Brask A, Kutter J P and Bruus H 2005 *Lab Chip* **5** 730–8
[13] Yao S H and Santiago J G 2003 *J. Colloid Interface Sci.* **268** 133–42
[14] Yao S H, Hertzog D E, Zeng S L, Mikkelsen J C and Santiago J G 2003 *J. Colloid Interface Sci.* **268** 143–53
[15] Ajdari A 2004 *C. R. Physique* **5** 539–46
[16] Brunet E and Ajdari A 2004 *Phys. Rev.* E **69** 016306
[17] Rice C L and Whitehead R 1965 *J. Phys. Chem.* **69** 4017–24
[18] Probstein R F 1994 *PhysicoChemical Hydrodynamics, an introduction* (New York: John Wiley)
[19] Mortensen N A and Bruus H 2005 *Preprint* http://physics/0511056
[20] Mortensen N A, Okkels F and Bruus H 2006 *Phys. Rev.* E **73** 012101
[21] Dirac P A M 1981 *The Principles of Quantum Mechanics* 4th edn (Oxford: Oxford University Press)
[22] Merzbacher E 1970 *Quantum Mechanics* (New York: Wiley)
[23] Batchelor G K 1967 *An Introduction to Fluid Dynamics* (Cambridge: Cambridge University Press)
[24] Landau L D and Lifshitz E M 1987 *Fluid Mechanics* vol 6 *Course of Theoretical Physics* 2nd edn (Oxford: Butterworth–Heinemann)
[25] Morse P M and Feshbach H 1953 *Methods of Theoretical Physics* (New York: McGraw-Hill)
[26] Parker R G and Mote C D 1998 *J. Sound Vib.* **211** 389–407
[27] Comsol support and Femlab documentation, www.comsol.com
[28] Brack M and Bhaduri R K 1997 *Semiclass. Phys.* (New York: Addison-Wesley)
[29] Bazant M Z, Thornton K and Ajdari A 2004 *Phys. Rev.* E **70** 021506
[30] Behrens S H and Grier D G 2001 *J. Chem. Phys.* **115** 6716–21